J. Fluid Mech. (2025), *vol.* 1009, A70, doi:10.1017/jfm.2025.259

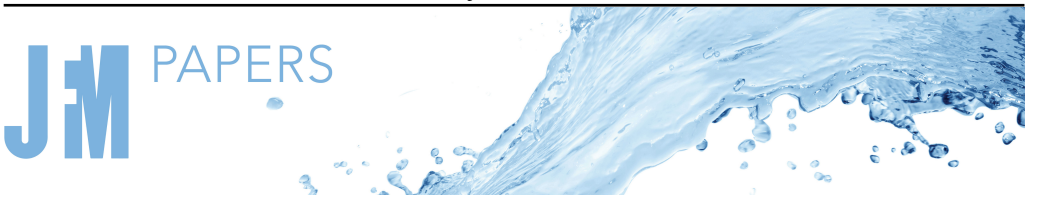

Force balances in spherical shell rotating convection

Souvik Naskar[1], **Chris Davies**[1], **Jon Mound**[1] **and Andrew Clarke**[1]

[1]School of Earth and Environment, University of Leeds, Leeds LS2 9JT, UK

Corresponding author: Souvik Naskar, s.naskar@leeds.ac.uk

(Received 12 August 2024; revised 19 December 2024; accepted 19 February 2025)

Significant progress has been made in understanding planetary core dynamics using numerical models of rotating convection (RC) in spherical shell geometry. However, the behaviour of forces in these models within various dynamic regimes of RC remains largely unknown. Directional anisotropy, scale dependence and the role of dynamically irrelevant gradient contributions in incompressible flows complicate the representation of dynamical balances in spherical shell RC. In this study, we systematically compare integrated and scale-dependent representations of mean and fluctuation forces and curled forces (which contain no gradient contributions) separately for the three components $(\hat{r}, \hat{\theta}, \hat{\phi})$. The analysis is performed with simulations in a range of convective supercriticality $Ra_T/Ra_T^c = 1.2-297$ where Ra_T and Ra_T^c are the Rayleigh and critical Rayleigh numbers, respectively and Ekman number $E = 10^{-3}-10^{-6}$, with fixed Prandtl number $Pr = 1$, along with no-slip and fixed flux boundaries. We have excluded regions from each boundary of the spherical shell, with a thickness equivalent to ten velocity boundary layers, which provides a consistent representation of the bulk dynamics between the volume-averaged force and curled force balance in the parameter space studied. Radial, azimuthal and co-latitudinal components exhibit distinct force and curled force balances. The total magnitudes of the mean forces and mean curled forces exhibit a primary thermal wind balance; the corresponding fluctuating forces are in a quasi-geostrophic primary balance, while the fluctuating curled forces transition from a Viscous–Archimedean–Coriolis balance to an Inertia–Viscous–Archimedean–Coriolis balance with increasing Ra_T/Ra_T^c. The curled force balances are more weakly scale-dependent compared to the forces, and do not show clear cross-over length scales. The fluctuating force and curled force balances are broadly consistent with three regimes of RC (weakly nonlinear, rapidly rotating and weakly rotating), but do not exhibit sharp changes with Ra_T/Ra_T^c, which inhibits the identification of precise regime boundaries from these balances.

Key words: geostrophic turbulence, rotating flows, Bénard convection

1. Introduction

Buoyancy-driven convection in a rotating spherical shell is a classical framework for studying the dynamics and magnetic field generation in the cores of planets and stars. However, despite significant progress (Gastine *et al.* 2016; Schaeffer *et al.* 2017; Long *et al.* 2020; Schwaiger *et al.* 2020; Gastine & Aurnou 2023), state-of-the-art direct numerical simulations cannot reach the parameter values that are representative of the astrophysical bodies, and are unlikely to do so in the near future (Davies *et al.* 2011; Roberts & King 2013). Therefore, extensive work has focused on developing scaling relations between the governing input parameters and global output diagnostic quantities of numerical simulations, which can be used to extrapolate to the conditions of planetary cores, and facilitate comparisons with available observations. These scaling relations rely on the balance of forces that determine the system dynamics (e.g. Christensen *et al.* 2010; King & Buffett 2013; Aubert *et al.* 2017), so it is crucial to quantify dynamical balances in numerical simulations accurately.

The dynamics in rotating non-magnetic convection are governed by the Ekman number E, a measure of the ratio of viscous to Coriolis forces, the Prandtl number Pr, the ratio of viscous to thermal diffusivities, and the Rayleigh number Ra_T, measuring the buoyancy force driving convection. Theoretical considerations suggest that the convecting system exhibits at least three distinct dynamical regimes (e.g. Aubert *et al.* 2001; King & Buffett 2013; King *et al.* 2013; Gastine *et al.* 2016; Aurnou *et al.* 2020; Long *et al.* 2020; Kunnen 2021). At fixed E and Pr, raising the thermal forcing to just above the onset of convection (i.e. $Ra_T \geqslant Ra_T^c$, where $Ra_T^c \propto E^{4/3}$ is the critical Rayleigh number at the onset of convection) leads to weakly nonlinear (WN) convection. In this regime, the primary dynamics is expected to be a quasi-geostrophic (QG) balance between Coriolis and pressure forces, while the residual (i.e. the ageostrophic Coriolis force) is balanced by buoyancy and viscous forces forming a secondary Viscous–Archimedean (buoyancy)–Coriolis (ageostrophic) or VAC balance. Increasing the thermal forcing increases the role of inertia, which leads to a turbulent rapidly rotating (RR) flow regime where strong nonlinearity and rotational constraint coexist. In this regime, both viscosity and inertial forces are expected to be small relative to the Coriolis force in the primary QG balance, with an Inertia–Archimedian–Coriolis (ageostrophic) or IAC balance generally assumed among the secondary forces. Further increase in thermal forcing leads to the weakly rotating (WR) regime where the primary QG balance is gradually broken, eventually resulting in non-rotating behaviour at sufficiently high Ra_T. Among these three regimes, the RR regime is thought to be more relevant for investigating planetary core convection, as compared to the other regimes (Kunnen 2021).

Depending on the dynamical balance, global and local flow diagnostic quantities (e.g. average velocity, length scale, heat transport, boundary layer thickness) may exhibit distinct scaling with the governing input parameters. Scaling regimes in rotating spherical shell convection have been studied extensively by Gastine *et al.* (2016) and Long *et al.* (2020) (henceforth referred to as L20). The conformity of the simulation diagnostics with theoretical scaling laws was utilized to demarcate boundaries between the dynamical regimes (i.e. WN, RR, WR). For example, Gastine *et al.* (2016) and L20 defined the WN regime based on the theoretical expectation that at low supercriticality, the Nusselt number Nu, representing the ratio of the total average heat flux from the shell to the conductive flux, scales as $Nu - 1 \propto Ra_T/Ra_T^c - 1$ (Gillet & Jones 2006). They found that this heat transfer behaviour is consistent with the dimensionless flow length scale scaling $\ell \sim E^{1/3}$ and Reynolds number scaling $Re \sim B^{1/2}E^{1/3}$ (where B is the convective power), as expected from a VAC balance. For higher supercriticality,

a length scale scaling $\ell \sim Ro^{1/2}$ (where Ro, the Rossby number, is a measure of the ratio of inertia and Coriolis forces) and a Reynolds number scaling $Re \sim B^{2/5}E^{1/5}$ are approached, indicating an IAC balance. The asymptotically reduced models of Guervilly *et al.* (2019) also found a 'diffusion-free' $\ell \sim Ro^{1/2}$ scaling. An asymptotically reduced plane layer model of convection (Oliver *et al.* 2023) found the scaling of Nu and Re consistent with IAC predictions, while the length scale remained viscously controlled (i.e. $\ell \sim E^{1/3}$). A rotating cylinder experiment (Abbate & Aurnou 2023), however, was unable to distinguish between a viscously controlled regime and a 'diffusion-free' regime from the scaling of the length scale. These comparisons relied on assumed force balances; however, the quantitative behaviour of forces in numerical simulations of spherical shell rotating convection (RC) remains largely unexplored. A few studies have explored force balances in plane layer geometries (Guzmán *et al.* 2020; Naskar & Pal 2022*a*,*b*), which may represent the dynamics in the tangent cylinder region of a spherical shell (Gastine & Aurnou 2023), while Schwaiger *et al.* (2020), Teed & Dormy (2023) and Nicoski *et al.* (2024) have computed force balances in a limited number of spherical shell RC runs. Hence the primary objective of our study is to investigate the dynamical balances that emerge in numerical simulations of spherical shell RC.

Quantifying dynamical balances in RC is an intricate issue. The force representation in incompressible flows is complicated by the existence of the gradient portions of forces, which are balanced by the pressure gradient term, but are not directly relevant to the dynamics (Hughes & Cattaneo 2019). A simple way to remove the gradient contributions is to curl the force balance (Dormy 2016), though the derivative operation can enhance small-scale contributions to the individual terms (Teed & Dormy 2023). Differences between the dynamics predicted by force and curled balances are important since some theoretical predictions consider the asymptotic behaviour of forces (Nicoski *et al.* 2024), whereas others are based on curled forces (e.g. VAC and IAC in L20). Teed & Dormy (2023) found that forces and their curls predicted different dynamical balances in a single simulation of rotating spherical shell convection. Here, we investigate the consistency between force and curled depictions of RC dynamics across a broad range of parameters ($Ra_T/Ra_T^c = 1.2{-}297$, $E = 10^{-3}{-}10^{-6}$ and $Pr = 1$).

When calculating forces or curls, it is crucial to distinguish dynamics in the boundary layers and the convective bulk. Integrating forces over the entire spherical shell may overestimate the role of viscosity in the bulk dynamics (Soderlund *et al.* 2012; Yadav *et al.* 2016). Most studies of force calculations remove a region corresponding to one velocity boundary layer (VBL) thickness at the top and bottom of the domain (e.g. Schwaiger *et al.* 2020; Teed & Dormy 2023; Nicoski *et al.* 2024) in order to isolate the bulk dynamics. However, we are unaware of previous systematic studies that have established the thickness of the layer near the boundaries that should be excluded from the volume-averaged forces/curls to obtain a robust estimate of the bulk dynamics.

In rotating spherical shell convection, the balance in the axisymmetric part of forces (corresponding to spherical harmonic order $m = 0$) can be different from the balance in their non-axisymmetric counterparts. Nicoski *et al.* (2024) partitioned the forces into azimuthally averaged and corresponding fluctuating parts, and analysed the scaling behaviour of the fluctuating radial forces as a function of E and Ra_T in RC with strong zonal flows, finding a primary QG balance across a broad range of parameters. In contrast to the QG force balance in the small-scale (i.e. $m \neq 0$) convective motions (Nicoski *et al.* 2024), Aubert (2005) focused on the large-scale dynamics and used curls to identify a horizontal thermal wind (TW) balance in the large-scale azimuthal ($m = 0$) motions for RC simulations operating in the RR regime. Here, we systematically compare mean and

fluctuating components of forces and their curls across different dynamical regimes of spherical shell RC.

In a spherical shell geometry, an additional difficulty in representing the system dynamics arises due to the dependence of each force and curl component $(\hat{r}, \hat{\theta}, \hat{\phi})$ on the spatio-temporal coordinates (r, θ, ϕ, t) and scale (spherical harmonic degree l and order m), as well as the governing parameters (Ra_T, E, Pr). Since the buoyancy force is radial while the system rotates about a vertical axis, different dynamical balances may be expected in the three orthogonal directions. Directional anisotropy of the force balance has been considered rarely in spherical shell models (for an exception, see Calkins *et al.* 2021), and forces are usually represented by their total magnitudes (Soderlund *et al.* 2012; Guzmán *et al.* 2021; Orvedahl *et al.* 2021). Studies of azimuthally averaged forces (Calkins *et al.* 2021) and curls (Aubert 2005) in dynamo simulations have indeed revealed a TW balance in the meridional plane with a Coriolis–Lorentz balance in the azimuthal direction. We complement these works by considering the balance of individual $(\hat{r}, \hat{\theta}, \hat{\phi})$ force components in rotating spherical shell convection.

The scale-dependence of the force balance in RC spherical shell simulations has been investigated by considering the force contributions from each spherical harmonic degree l. Schwaiger *et al.* (2020) found a secondary balance between ageostrophic Coriolis and buoyancy forces at low l, and a cross-over to Coriolis–Inertia balance at higher l. They argued that the length scale at which inertia and buoyancy forces cross over is related to energetic scales of the flow, as estimated from the peak of the poloidal kinetic energy spectra. However, the scale-dependent representation of curled forces may not exhibit such a dynamically relevant cross-over scale (Teed & Dormy 2023). Furthermore, some simulations show that the small-scale curled balance differs markedly compared to the force balance (Teed & Dormy 2023). It is therefore useful to systematically compare the scale-dependent nature of force and curled balances in different dynamical regimes of RC.

In summary, previous studies have investigated various aspects of dynamical balances (e.g. forces versus curls, mean versus fluctuating balances, components versus combined terms, scale-dependence) in spherical shell RC. However, to our knowledge, no study systematically compares the different depictions of dynamical balances in different regimes of spherical shell RC. A recent related study by Nicoski *et al.* (2024) investigated the behaviour of fluctuating radial forces in spherical shell RC with fixed temperature and free-slip boundaries for $E = 5 \times 10^{-4} - 5 \times 10^{-7}$, $Pr = 1$ and the convective supercriticality range $Ra_T/Ra_T^c = 3-161$. They found a primary QG balance in the radial fluctuating forces at all parameters considered. At low convective supercriticalities, they obtained a secondary balance between buoyancy and ageostrophic Coriolis forces, while inertia and viscosity enter the balance at higher thermal forcing. In this paper, we systematically compare integrated and scale-dependent representations of mean and fluctuating forces and curled balances in the large suite of rotating spherical shell convection simulations from Mound & Davies (2017) and L20, supplemented by three new simulations. In contrast to Nicoski *et al.* (2024), our simulations use no-slip, fixed heat flux boundaries.

This paper is organized as follows. We present the mathematical model in § 2.1, the numerical details in § 2.2, and the force calculation method in § 2.3. Results are presented in § 3, beginning in § 3.1 with an analysis of the boundary region that must be excluded to ensure a robust representation of the bulk dynamics. In §§ 3.2 and 3.3, we investigate mean and fluctuating bulk-integrated force and curl balances, respectively. The total magnitude of the forces and their scale dependence are discussed in § 3.4. In § 4, we compare transitions in the computed force and curled balanced to the regime diagram obtained by L20. We discuss our observations and summarize the findings in § 5.

2. Method

2.1. *Mathematical model*

We employ a numerical model of convection of a Boussinesq fluid in a rotating spherical shell. The relevant physical properties of the fluid are the kinematic viscosity ν, thermal expansivity α, and thermal diffusivity κ, defined as $\kappa = k/\rho_0 c_p$, where k is the thermal conductivity, ρ_0 is the reference density, and c_p is the specific heat capacity. A spherical coordinate system (r, θ, ϕ) is used to represent the domain bounded by the inner and outer boundaries, r_i and r_o, respectively. The system rotates with a constant angular velocity $\boldsymbol{\Omega} = \Omega\hat{\boldsymbol{z}}$, about the vertical, and gravity g varies linearly with radius, with $g = g_o$ at the outer radius. The governing equations are cast in non-dimensional form using the shell gap h as the length scale, the viscous diffusion time h^2/ν as the time scale, and β/h as the temperature scale, giving

$$\boldsymbol{\nabla}\cdot\boldsymbol{u} = 0, \tag{2.1}$$

$$\frac{\partial \boldsymbol{u}}{\partial t} + (\boldsymbol{u}\cdot\boldsymbol{\nabla})\boldsymbol{u} + \frac{1}{E}\left(\hat{\boldsymbol{z}}\times\boldsymbol{u}\right) = -\boldsymbol{\nabla}\widetilde{P} + \left(\frac{Ra}{Pr}\right) T\boldsymbol{r} + \nabla^2\boldsymbol{u}, \tag{2.2}$$

$$\frac{\partial T}{\partial t} + (\boldsymbol{u}\cdot\boldsymbol{\nabla})(T + T_c) = \frac{1}{Pr}\nabla^2(T + T_c), \tag{2.3}$$

where T is the temperature fluctuation relative to the conductive state T_c, given by $\partial T_c/\partial r = -\beta/r^2$. The parameter β is related to the fixed heat flow through the boundaries as $Q = 4\pi\beta k$. No-slip velocity conditions and fixed heat flux temperature conditions have been used at both boundaries.

The non-dimensional numbers appearing in these equations are the Ekman number (E), Rayleigh number (Ra), and Prandtl number (Pr), which are defined as

$$E = \frac{\nu}{2\Omega h^2}, \quad Ra = \frac{g_o\alpha\beta h^3}{\nu\kappa r_o^*}, \quad Pr = \frac{\nu}{\kappa}. \tag{2.4}$$

Here, $r_o^* = 1/(1-\eta)$ is the non-dimensional outer radius, where $\eta = r_i/r_o$ is the radius ratio fixed at $\eta = 0.35$.

2.2. *Numerical details*

The velocity field is represented by toroidal and poloidal scalar fields, which are expressed as radially varying Schmidt-normalized spherical harmonics. Radial variations are expressed using second-order finite differences on the zeros of Chebyshev polynomials. A predictor–corrector scheme is used for time stepping in spectral space that treats the diffusion terms implicitly. Further numerical details can be found in previous studies that use the same solver (Willis *et al.* 2007; Davies *et al.* 2011; Matsui *et al.* 2016).

We consider all the simulations reported in Mound & Davies (2017) for $E = 10^{-4}$, 10^{-5} and 10^{-6}, that impose homogeneous heat flux at the outer boundary. The simulations performed by L20 at $E = 10^{-3}$, $E = 3\times10^{-4}$ and $E = 3\times10^{-5}$ are also included. It should be noted here that the flux Rayleigh number in this study relates to the modified flux Rayleigh number defined by Mound & Davies (2017) and L20 as $\widetilde{Ra} = Ra\,E$. To complement the database, we have run three more simulations at $E = 10^{-6}$, for $\widetilde{Ra} =$ 350, 550, 30 000. The details of these simulations are given in Appendix A. The Prandtl number is fixed at $Pr = 1$ for all runs. The fixed temperature Rayleigh number (Ra_T) is related to the fixed flux Rayleigh number (Ra) as

$$Ra_T = \frac{Ra}{Nu}\,\frac{(1-\eta)^2}{\eta}. \tag{2.5}$$

The reduced fixed-temperature Rayleigh number used in § 3 is defined as $\widetilde{Ra}_T = Ra_T\, E^{4/3}$. The critical values for the three definitions of Rayleigh numbers ($\widetilde{Ra}^c$, Ra_T^c and $\widetilde{Ra}_T^c$) at the onset of thermal convection are provided in Appendix B, based on the analysis of L20.

2.3. *Force calculation*

We refer to the terms from left to right in (2.2) as time derivative (TD), inertia (I), Coriolis (C), pressure gradient (P), thermal buoyancy (or Archimedean, A) and viscous (V) forces. Additionally, the ageostrophic Coriolis force $(1/E)(\hat{\boldsymbol{z}}\times\boldsymbol{u}) + \boldsymbol{\nabla}\widetilde{P}$ is denoted as C_{ag}. Henceforth, we use these abbreviations to refer to the balance in the simulations. For example, a balance between inertia, Archimedean (i.e. thermal buoyancy) and Coriolis forces will be referred to as an IAC balance. Also, a TW balance refers to an ACP force balance or an AC balance of curled forces. Similarly, a QG balance refers to a CP balance of forces.

We partition dependent variables into their azimuthally averaged mean and corresponding fluctuating parts as

$$\begin{aligned} f(r,\theta,\phi,t) &= \overline{f}(r,\theta,t) + f'(r,\theta,\phi,t),\\ \overline{f}(r,\theta,t) &= \frac{1}{2\pi}\int_0^{2\pi} f(r,\theta,\phi,t)\,\mathrm{d}\phi. \end{aligned} \tag{2.6}$$

In spectral representation, this is equivalent to partitioning into the azimuthally symmetric harmonics of order $m=0$ (mean) and the corresponding part with order $m\neq 0$. Azimuthally averaging (2.2) leads to

$$\underbrace{\frac{\partial\overline{\boldsymbol{u}}}{\partial t}}_{\overline{T}\,\overline{D}} + \underbrace{(\overline{\boldsymbol{u}}\cdot\boldsymbol{\nabla})\overline{\boldsymbol{u}}}_{I^{mm}} + \underbrace{\overline{(\boldsymbol{u}'\cdot\boldsymbol{\nabla})\boldsymbol{u}'}}_{\overline{I^{ff}}} + \underbrace{\frac{1}{E}\left(\hat{\boldsymbol{z}}\times\overline{\boldsymbol{u}}\right)}_{\overline{C}} = \underbrace{-\boldsymbol{\nabla}\overline{P}}_{\overline{P}} + \underbrace{\frac{Ra}{Pr}\overline{T}\,\boldsymbol{r}}_{\overline{A}} + \underbrace{\boldsymbol{\nabla}^2\overline{\boldsymbol{u}}}_{\overline{V}}, \tag{2.7}$$

where partitioning the mean inertial force term $\overline{I} = \overline{(\boldsymbol{u}\cdot\boldsymbol{\nabla})u}$ as $\overline{I} = I^{mm} + \overline{I^{ff}}$ leads to the mean–mean inertia term $I^{mm} = (\overline{\boldsymbol{u}}\cdot\boldsymbol{\nabla})\overline{\boldsymbol{u}}$ and the Reynolds stress $\overline{I^{ff}} = \overline{(\boldsymbol{u}'\cdot\boldsymbol{\nabla})\boldsymbol{u}'}$. Subtracting the mean momentum equation (2.7) from (2.2) leads to the corresponding fluctuating part of the momentum equation:

$$\begin{aligned} &\underbrace{\frac{\partial\boldsymbol{u}'}{\partial t}}_{T\,D'} + \underbrace{(\overline{\boldsymbol{u}}\cdot\boldsymbol{\nabla})\boldsymbol{u}'}_{I^{mf}} + \underbrace{(\boldsymbol{u}'\cdot\boldsymbol{\nabla})\overline{\boldsymbol{u}}}_{I^{fm}} + \underbrace{(\boldsymbol{u}'\cdot\boldsymbol{\nabla})\boldsymbol{u}'}_{I^{ff}} - \underbrace{\overline{(\boldsymbol{u}'\cdot\boldsymbol{\nabla})\boldsymbol{u}'}}_{\overline{I^{ff}}} + \underbrace{\frac{1}{E}\left(\hat{\boldsymbol{z}}\times\boldsymbol{u}'\right)}_{C'}\\ &\qquad = \underbrace{-\boldsymbol{\nabla}P'}_{P'} + \underbrace{\frac{Ra}{Pr}T'\,\boldsymbol{r}}_{A'} + \underbrace{\boldsymbol{\nabla}^2\boldsymbol{u}'}_{V'}, \end{aligned} \tag{2.8}$$

where the fluctuating inertial term I' has four parts, $I' = I^{mf} + I^{fm} + I^{ff} - \overline{I^{ff}}$, signifying the mean–fluctuating, fluctuating–mean, fluctuating–fluctuating inertial terms and the Reynolds stress. Among the fluctuating inertial terms in (2.8), the fluctuating–fluctuating term (I^{ff}) always dominates in our simulations. Therefore, we have discussed only the sum of the four terms I', for presentational convenience. The spherical harmonic degree $l=0$ of the mean radial forces and I^{ff} are balanced by the hydrostatic part of

the pressure gradient, which is irrelevant to the convective dynamics (Calkins *et al.* 2021; Nicoski *et al.* 2024). Therefore, we remove the degree $l = 0$ from the radial component of I^{ff} from (2.8), and from all the radial mean forces in (2.7). In our calculations, the temporally averaged values of TD terms in (2.7) and (2.8) remain small compared to all the other terms, though they may be significant for simulations with free-slip boundaries (Nicoski *et al.* 2024). Therefore, this term is not discussed in the next section, and the nonlinear advection terms are referred to as inertia throughout the text. Also, the abbreviations of mean (fluctuating) forces are mentioned explicitly rather than using an overbar (or prime). For example, a VAC balance in the fluctuating curled forces will be referred to as a curled fluctuating VAC balance, rather than a V′A′C′ balance of curled forces.

The total force magnitude can be calculated from the vector components as

$$f_{tot} = |\boldsymbol{f}| = \sqrt{f_r^2 + f_\theta^2 + f_\phi^2}, \tag{2.9}$$

where f_r, f_θ and f_ϕ are the components in the $\hat{r}$, $\hat{\theta}$ and $\hat{\phi}$ directions, respectively. Further, the force components (or the total force magnitude) are represented by their root mean square (r.m.s.) values, where the 'mean' refers to a volume average performed by first averaging over a spherical surface and then averaging in the radial direction excluding regions near the boundary:

$$\langle f_j \rangle_{\mathcal{S}} = \frac{1}{4\pi r^2} \int_0^{\pi} \int_0^{2\pi} f_j(r, \theta, \phi, t)\, r^2 \sin\theta \, \mathrm{d}\phi \, \mathrm{d}\theta, \tag{2.10a}$$

$$\langle f_j \rangle_{\mathcal{V}} = \frac{1}{h - r_{ex}\delta_v^i - r_{ex}\delta_v^o} \int_{r_i + r_{ex}\delta_v^i}^{r_o - r_{ex}\delta_v^o} \langle f_j \rangle_{\mathcal{S}} \, \mathrm{d}r, \tag{2.10b}$$

where $j = r, \theta, \phi$ or *tot*. In (2.10*b*), r_{ex} represents the multiple of the VBL thicknesses at the inner and the outer boundaries, δ_v^i and δ_v^o, respectively, that we exclude from the volume average to ensure the representation of bulk dynamics. There are two common methods of estimating the thickness of the VBL from the radial profile of horizontal velocity (L20). One is the 'local maxima method' (L20), where the distance of the nearest maximum in this profile from the respective boundaries is defined as the VBL thickness, whereas the distance of the intersection of the tangent to the profile at the wall and the tangent at the nearest maximum near the wall is used as VBL thickness in the 'linear intersection method' (Gastine *et al.* 2016). In our study, VBL thickness is estimated using the linear intersection method, which has been reported as a better estimate than the local maxima method (Gastine *et al.* 2015). The value of r_{ex} is determined in § 3.1.

We evaluate the scale dependence of the forces as a function of spherical harmonic degree following Aubert *et al.* (2017). The volume-averaged r.m.s. forces are averaged in time over at least a hundred advective time units after the simulations reach a statistically stationary state (Mound & Davies 2017; Long *et al.* 2020). The calculation of forces follows the methodology reported by Calkins *et al.* (2021) and Nicoski *et al.* (2024), and a couple of cases from Nicoski *et al.* (2024) have been reproduced to validate our force calculation.

3. Results

In this section, we investigate the force balances in the thermally driven RC simulations at $E = 10^{-5}$ reported in Mound & Davies (2017) and L20. We start, in § 3.1, with a systematic study to assess the thickness of the region near the boundaries that should

be excluded to ensure the representation of bulk dynamics. We explore the mean and fluctuating parts of each component of forces in § 3.2, and their curl in § 3.3. The scale dependence of the forces is investigated in § 3.4, whereas the role of inertia in the force balance in various regimes of RC is considered in § 4. The thermal forcings at which transitions occur from WN to RR to WR behaviours have been predicted previously based on theoretical scaling laws (L20) and are marked by vertical lines in the volume-averaged balances presented in the next section. We use representative cases from each of these regimes at $\widetilde{Ra} = 90$ (WN), $\widetilde{Ra} = 1200$ (RR) and $\widetilde{Ra} = 13000$ (WR) to establish the required boundary layer exclusion in § 3.1 and to demonstrate the scale dependence of the balances in § 3.4. The force balances at $E = 10^{-4}$ and $E = 10^{-6}$ are presented in supplementary figures S1 and S2, respectively, for comparison.

3.1. *Boundary layer exclusion*

We begin by assessing the variation of the fluctuating forces (figures 1*c*,*e*,*g*) and their curls (figures 1*d*,*f*,*h*) as a function of r_{ex}, which represents the number of VBLs excluded near each boundary from the volume average. Mean quantities exhibit similar behaviour, so we focus on fluctuating quantities in this subsection. A common practice (e.g. Yadav *et al.* 2016; Aubert *et al.* 2017) is to exclude a single VBL before calculating the volume average (figures 1*a*,*b*), which corresponds to $r_{ex} = 1$. We demonstrate the impact of changing r_{ex} in our representative cases from the WN (figures 1*c*,*d*), RR (figures 1*e*,*f*) and WR (figures 1*g*,*h*) regimes. Since viscous forces are strongest near the no-slip boundaries in our simulations, that force term changes most significantly as boundary layers are excluded (figures 1*c*,*e*,*g*). The viscous force term decreases with increasing r_{ex} and converges to its bulk values for $r_{ex} \geqslant 5$ for all cases. The curled viscous force requires more exclusion than the uncurled force to converge to its bulk values (e.g. compare figures 1*c*,*d*), probably due to the presence of an extra spatial gradient that inflates sharp changes near the boundaries.

Crucially, excluding only a single VBL to calculate the forces is generally insufficient to properly capture bulk dynamics in our simulations. In the WN regime, the viscous force is larger than inertia for $r_{ex} = 1$ (figure 1*c*), while it falls below inertia for $r_{ex} > 2$. Overestimation of the viscous term in the bulk with $r_{ex} = 1$ is particularly problematic when considering curled forces, where it can result in a more than an order of magnitude overestimate (e.g. figure 1*d*). In the curled forces, a VC balance is obtained for the WN cases using $r_{ex} = 1$, whereas an AC (or TW) balance can be observed for $r_{ex} = 10$ (figure 1*d*). In the RR regime (figure 1*f*), the curled force balance changes from VC to IVAC with increasing exclusion. For the WR case (figure 1*h*), the IVC balance obtained for $r_{ex} = 1$ becomes an IVAC balance with increasing r_{ex}. Figure 1 also shows that the ordering of terms in the force and curled balances can differ significantly at low r_{ex}, but show better agreement for large r_{ex}.

To test the appropriate value of r_{ex} across the entire suite of runs, we plot the ratio of volume-averaged fluctuating viscous to Coriolis terms as a function of r_{ex} in figure 2. This ratio is generally largest for low r_{ex}, and decreases with increasing r_{ex}. The value of r_{ex} required to obtain converged results (i.e. that do not change upon a further increase in r_{ex}) varies somewhat with the parameters, but is always larger for the curled terms than the forces. Across our suite of simulations, a converged bulk force balance is always obtained with $r_{ex} \geqslant 5$. The curled force ratio (figure 2*b*) exhibits slower convergence to the bulk values than the uncurled forces, and can require $r_{ex} \geqslant 10$. Following the analysis in figure 2, we exclude ten VBLs (i.e. $r_{ex} = 10$) in all volume averages. This corresponds to 2−4 VBLs if the local maxima method is used instead of a linear intersection method, as the former leads to thicker estimates of the VBL (Gastine *et al.* 2015). For the thickest

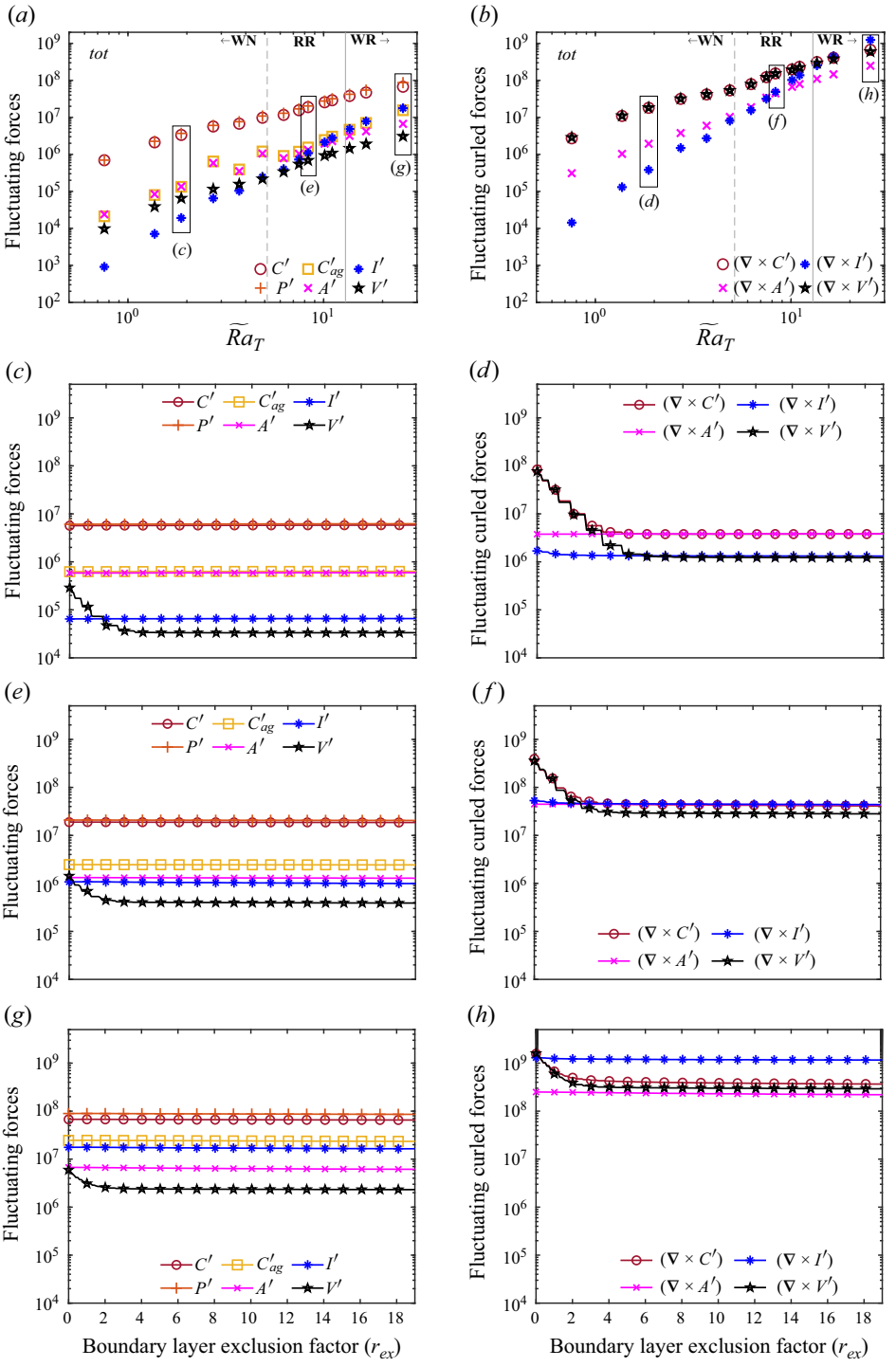

Figure 1. Variation of volume-averaged r.m.s. fluctuating forces (left-hand column) and their curls (right-hand column) at $E = 10^{-5}$ with thermal forcing $\widetilde{Ra}_T$ where only single boundary layer thicknesses are excluded ($r_{ex} = 1$) in (*a*,*b*), and with boundary layer exclusion factor (r_{ex}) in (*c*–*h*) for the annotated cases in (*a*,*b*). The representative cases from WN, RR and WR regimes correspond to (*c*,*d*) $\widetilde{Ra} = 150$, (*e*,*f*) $\widetilde{Ra} = 1200$ and (*g*,*h*) $\widetilde{Ra} = 13\,000$.

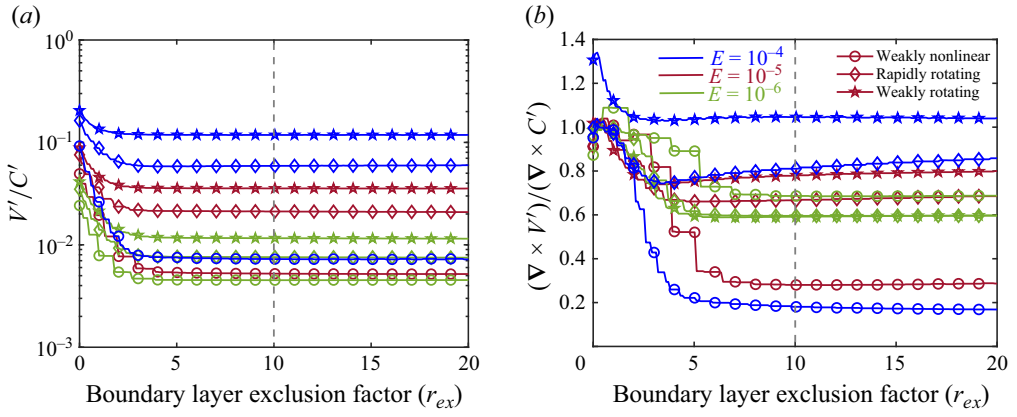

Figure 2. Variation of fluctuating viscous to Coriolis (*a*) force and *(b)* curled force ratios, with the thickness of the excluded layers as a multiple (r_{ex}) of VBL thickness. The representative cases from WN (circles), RR (diamonds) and WR (stars) regimes for three Ekman numbers correspond to $\widetilde{Ra} = 30, 900, 13\,000$ for $E = 10^{-4}$ (blue), $\widetilde{Ra} = 90, 1200, 13\,000$ (red) for $E = 10^{-5}$ and $\widetilde{Ra} = 150, 2000, 18\,000$ for $E = 10^{-6}$ (green).

boundary layers at $\widetilde{Ra} = 30$ and $E = 10^{-4}$, approximately 34−38 % of the gap is excluded from the radial extent of the domain at $r_{ex} = 10$. For the majority of simulations, the total excluded region amounts to less than 20 % of the gap width.

3.2. *Force balance*

The volume-averaged mean and fluctuating forces as functions of thermal forcing $\widetilde{Ra}_T$ are shown in figures 3(*a*,*c*,*e*) and 3(*b*,*d*,*f*), respectively. Because buoyancy acts only radially, and the Coriolis force is horizontal, there will be a directional anisotropy in the force balances, therefore we consider the radial ($\hat{r}$, figures 3*a*,*b*), co-latitudinal ($\hat{\theta}$, figures 3*c*,*d*), and azimuthal ($\hat{\phi}$, figures 3*e*,*f*) force components separately.

In the radial direction (figure 3*a*), we find a primary TW balance between the mean Coriolis, pressure and buoyancy forces, with the buoyancy force gradually becoming subdominant at the highest values of $\widetilde{Ra}_T$ considered. In the θ direction (figure 3*c*), the primary balance in the mean forces is QG (i.e. between Coriolis and pressure forces) for all $\widetilde{Ra}_T$. These mean balances in $\hat{r}$ and $\hat{\theta}$ are the same as the balances reported in recent dynamo simulations (Calkins *et al.* 2021). The residuals of the primary TW balance in $\hat{r}$ and the primary QG balance in $\hat{\theta}$ are balanced by the Reynolds stress ($\overline{I^{ff}}$), which dominates the two components of the total mean advection term ($\overline{I} = \overline{I^{mm}} + \overline{I^{ff}}$) until the largest forcings considered. In the mean $\hat{r}$ and $\hat{\theta}$ balances, viscosity is always subdominant, as found by Calkins *et al.* (2021). The primary mean forces in the azimuthal direction (figure 3*e*) have similar magnitude with the secondary forces in the $\hat{r}$ and $\hat{\theta}$directions. Owing to our choice of averaging, there is no mean pressure gradient or buoyancy force in the azimuthal direction. Therefore, the Coriolis force is balanced by inertia and viscous forces at low $\widetilde{Ra}_T$ (IVC balance), whereas an IC balance dominates at high $\widetilde{Ra}_T$.

In the fluctuating forces in figures 3(*b*,*d*,*f*), the QG balance between Coriolis and pressure forces dominates in all directions. At low $\widetilde{Ra}_T$ in the radial direction, there is a secondary AC_{ag} balance between ageostrophic Coriolis force and buoyancy, with viscosity approximately an order of magnitude weaker. At high $\widetilde{Ra}_T$ in the radial direction, there is a secondary IAC_{ag} balance, with viscosity still subdominant but less than an order of

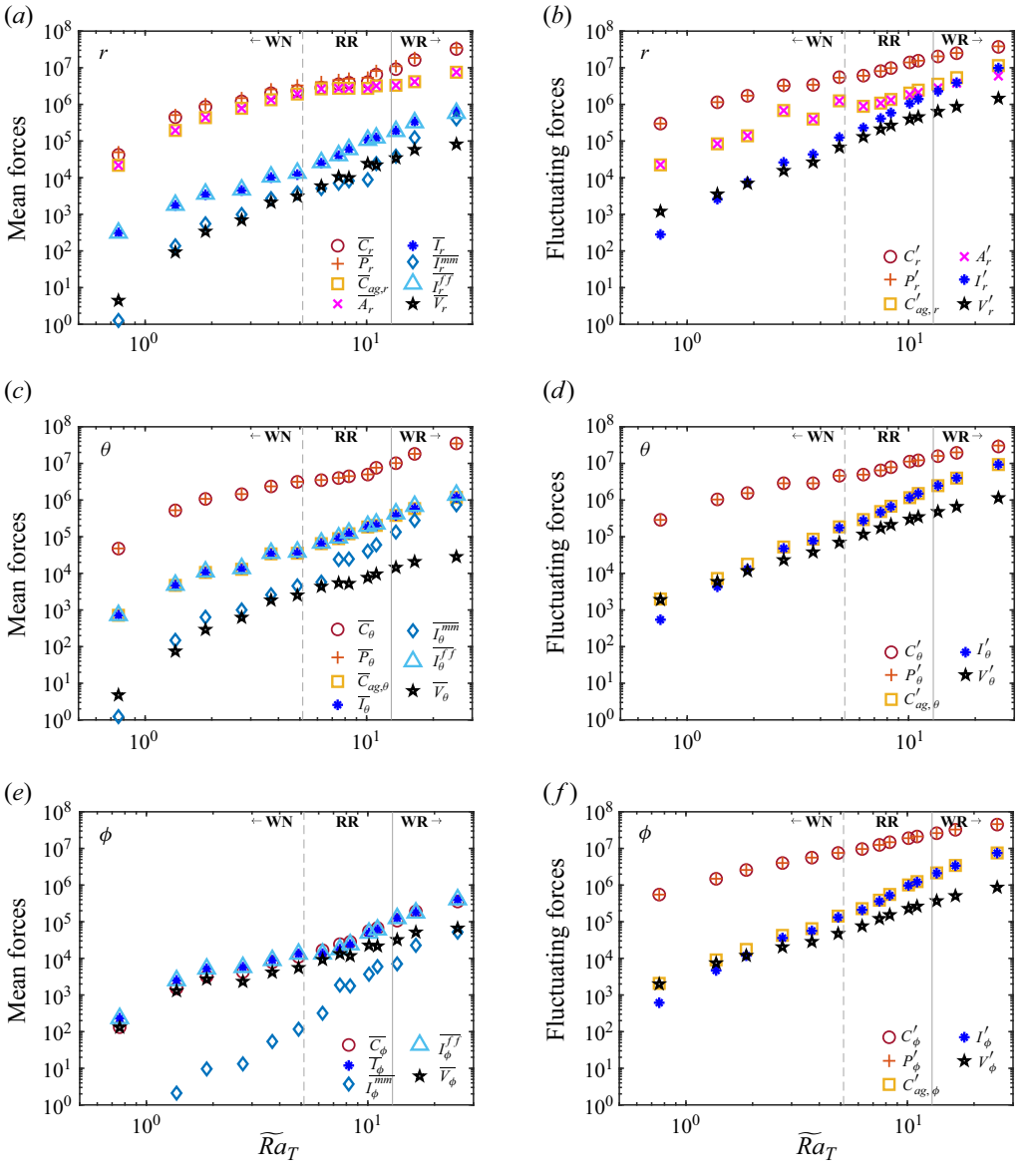

Figure 3. Volume-averaged r.m.s. mean (left-hand column) and fluctuating (right-hand column) force components in (*a,b*) $\hat{r}$, (*c,d*) $\hat{\theta}$ and (*e,f*) $\hat{\phi}$ for $E = 10^{-5}$.

magnitude weaker. In the θ and ϕ directions, the ageostrophic Coriolis force is balanced by both viscous and inertial forces for low $\widetilde{Ra}_T$ (IVC$_{ag}$ balance), with the relative importance of viscosity weakening as $\widetilde{Ra}_T$ increases.

The behaviour of the fluctuating radial forces can be compared with the free-slip and fixed temperature simulations of Nicoski *et al.* (2024) (see figure 16(*b*) in their paper). For both studies, the primary radial balance is QG, while the secondary balance is AC$_{ag}$ at low thermal forcings, and IAC$_{ag}$ with a weakly subdominant viscous contribution at higher thermal forcings. Though the viscous force can be higher than inertia for the lowest $\widetilde{Ra}_T$

values considered here (figure 3*b*), it is the smallest force in both studies when the same range of $\widetilde{Ra}_T$ is considered. However, the two studies find different dominant contributions to the inertia force. Figure 3(*b*) shows that I' is dominated by I^{ff}, which balances C_{ag} and A'_r for large $\widetilde{Ra}_T$. In contrast, Nicoski *et al.* (2024) found that the mean-fluctuating inertia (I^{mf}) dominates the nonlinear advection terms, which, combined with the TD, balances C_{ag} and A'_r for large $\widetilde{Ra}_T$. This difference probably arises from the strong mean zonal flows in the simulations of Nicoski *et al.* (2024), owing to the use of free-slip conditions.

The partitioning into mean ($m = 0$) and fluctuating ($m \neq 0$) forces brings out distinct balances (comparing the left-hand and right-hand plots of figure 3). For example, the radial force balance exhibits a primary mean TW balance and a primary fluctuating QG balance. The unpartitioned (i.e. mean + fluctuating) radial force balance has a primary QG balance that exceeds a subdominant AC_{ag} balance by a factor 2−3, essentially averaging the large- and small-scale dynamics.

The azimuthal component of azimuthally averaged forces has been considered in previous studies (Sheyko *et al.* 2018; Menu *et al.* 2020) since it removes the pressure gradient, although there is no buoyancy force in this direction. Our analysis indicates that this representation (see figure 3(*e*) for an example) does not reflect the balance of mean forces in the $\hat{r}$ and $\hat{\theta}$ directions, and also does not correspond to the balances of the fluctuating part of the forces.

3.3. *Curled force balance*

Though the force balance provides useful insights into the dynamics, all forces in (2.2) are non-solenoidal and therefore will have gradient portions. These gradient portions of the forces are balanced by the pressure gradient term, which plays no role in the dynamics (Hughes & Cattaneo 2019; Teed & Dormy 2023). Our approach to removing these gradients is to take the curl of the momentum equation. We partition the curled forces into mean (figures 4*a*,*c*,*e*) and fluctuating (figures 4*b*,*d*,*f*) parts, and separately consider the radial (figures 4*a*,*b*), co-latitudinal (figures 4*c*,*d*), and azimuthal (figures 4*e*,*f*) components. Since the buoyancy force is radial, its curl acts only in the angular directions (θ and ϕ), making the curled balance inherently anisotropic.

In the $\hat{r}$ and $\hat{\theta}$ directions, we find a primary mean balance between the Coriolis, inertial and viscous terms (IVC balance), with the viscous contribution weakening at the highest values of $\widetilde{Ra}_T$ considered. In the $\hat{\phi}$ direction, the mean balance is a TW, except at the highest values of $\widetilde{Ra}_T$ considered, where the mean curled inertia also enters this primary balance. A TW arises only in the mean azimuthal component because our choice of averaging causes the θ-component of the mean curled buoyancy force to vanish (since $\partial \overline{T}/\partial \phi = 0$). Aubert (2005) also found a TW balance in the azimuthally averaged curled force balance for non-magnetic simulations at $E = 10^{-4}$–10^{-5}.

The curled fluctuating forces in $\hat{\theta}$ and $\hat{\phi}$ exhibit a primary balance between Coriolis, buoyancy and viscous terms (VAC balance) at low $\widetilde{Ra}_T$, while the inertial force gradually enters this balance with increasing $\widetilde{Ra}_T$. A similar trend is observed in the radial balance, except for the omission of the buoyancy term. We note here that the radial curled force balance, as reported by Dormy (2016), may not represent the curled force balance in the other directions.

As with the forces, partitioning curled terms into mean and fluctuating components brings out distinct balances that would be obscured if only the unpartitioned curled terms were considered. In particular, because the fluctuating curled quantities have much higher amplitude than the mean curled quantities, an unpartitioned (i.e. mean + fluctuation) curled force representation would simply show the fluctuating small-scale balance.

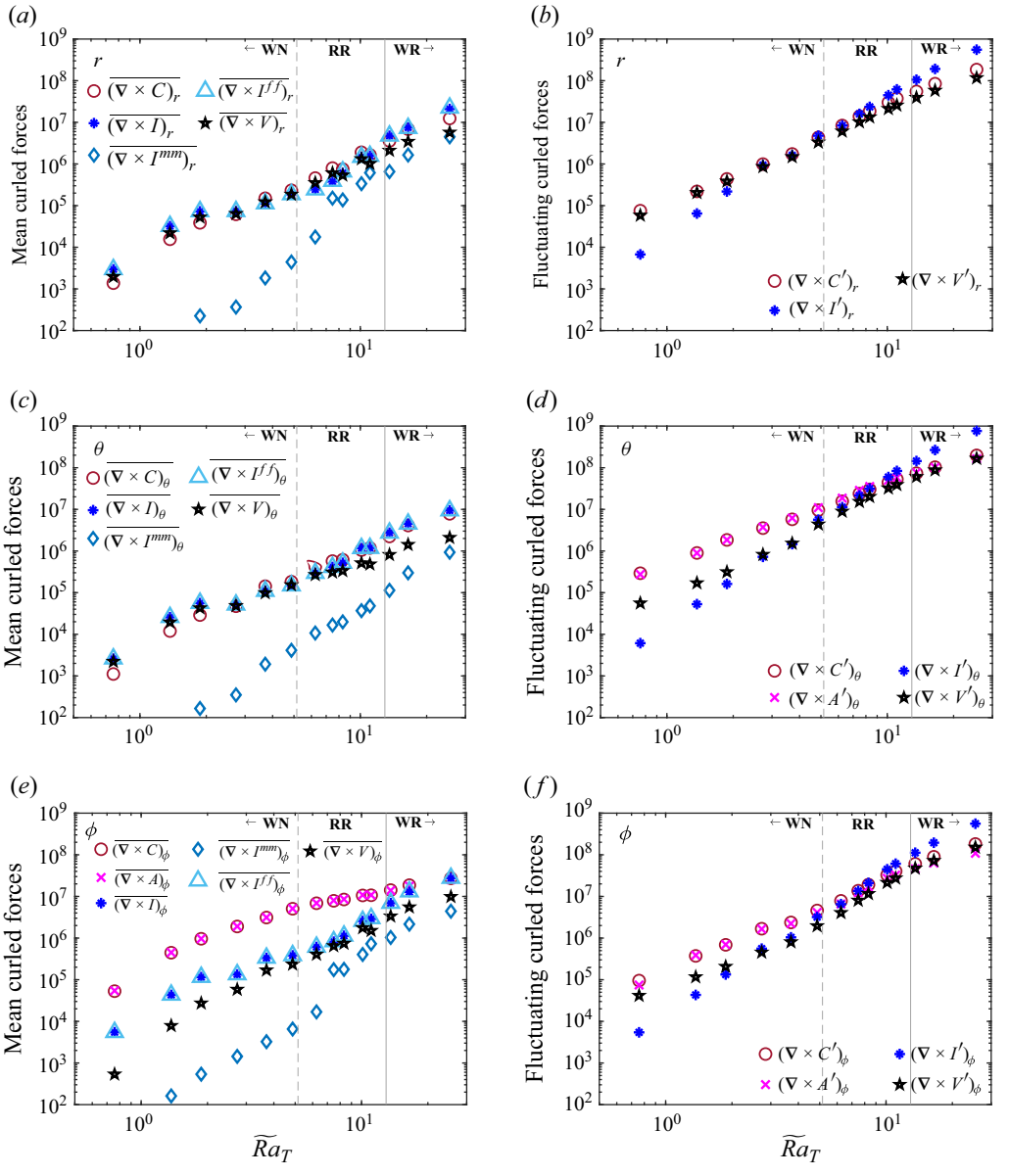

Figure 4. Volume-averaged r.m.s. mean (left-hand column) and fluctuating (right-hand column) curled force components in (a,b) $\hat{r}$, (c,d) $\hat{\theta}$ and (e,f) $\hat{\phi}$ for $E = 10^{-5}$.

The balance obtained from the total magnitude of the three mean curled components follows the balance in the $\hat{\phi}$ direction shown in figure 4(e), while the balance obtained from the total magnitude of the three fluctuating curled components reflects the balances in the $\hat{\theta}$ and $\hat{\phi}$ directions shown in figures 4(d) and 4(f).

3.4. *Scale-dependent force balance*

In figure 5, we compare the scale dependence of the total magnitude of the fluctuating forces (left-hand column) and their curls (right-hand column) with the corresponding

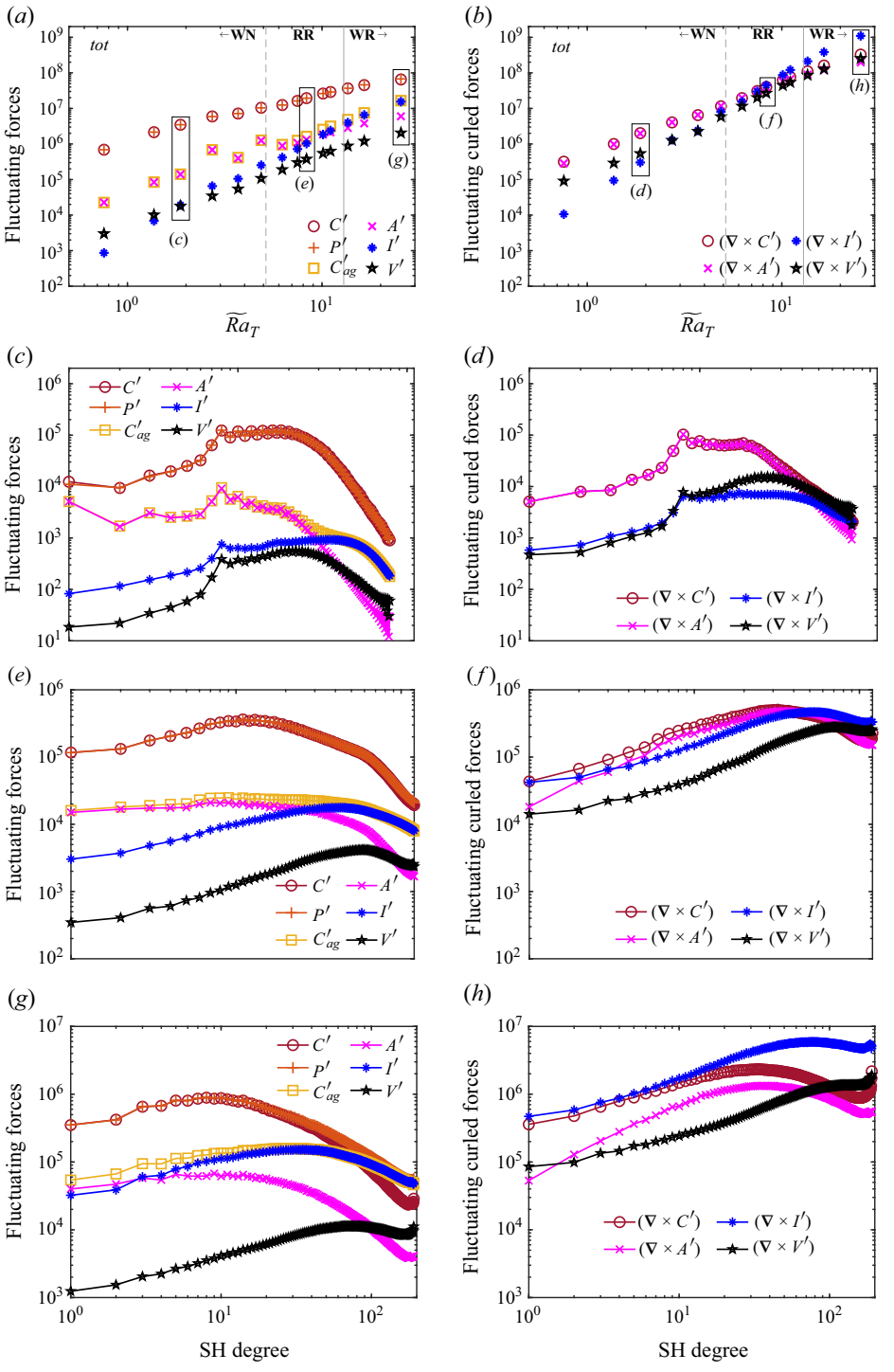

Figure 5. Volume-averaged r.m.s. of the total magnitude of fluctuating forces (left-hand column) and their curls (right-hand column) at $E = 10^{-5}$ as a function of thermal forcing $\widetilde{Ra}_T$ in (*a*,*b*) and with SH degree (l) in (*c–h*) for the exemplar cases highlighted in (*a*,*b*). The representative cases from WN, RR and WR regimes correspond to (*c*,*d*) $\widetilde{Ra} = 90$, (*e*,*f*) $\widetilde{Ra} = 1200$ and (*g*,*h*) $\widetilde{Ra} = 13\,000$.

scale-integrated representation (figures 5*a*,*b*). For brevity, we again select one case from each of the WN (figures 5*c*,*d*), RR (figures 5*e*,*f*), and WR (figures 5*g*,*h*) regimes, corresponding to $\widetilde{Ra} = 90, 1200, 13\,000$, respectively (these cases are highlighted in figures 5*a*,*b*). The regime boundaries are shown using dashed and solid vertical lines, following the analysis of L20, as described in detail in the next subsection. Although the mean forces are also dependent on the spherical harmonic (SH) degree, we focus on the fluctuating forces because of their more direct correspondence with the convective motions and the heat transfer behaviour.

Based on the scale-integrated fluctuating forces, all simulations have a QG primary balance (figure 5*a*). This primary force balance holds across all scales in the WN and RR regimes (figures 5*c*,*e*), while inertia enters the primary balance at the small scales (i.e. large l) in the WR regime (figure 5*g*). The secondary force balance in the WN and RR regimes is characterized by an AC_{ag} balance between buoyancy and ageostrophic Coriolis at large scales, with inertia entering at small scales (figure 5*e*). In the WR regime, there is a secondary IAC_{ag} balance with a significant inertial contribution at all scales. The scale dependence of forces in the RR regime (figure 5*e*) is similar to the force spectra reported in Schwaiger *et al.* (2020) (see figure 7(*a*) in their paper) and is often referred to as a QG–IAC_{ag} balance.

Previous studies have attempted to relate crossings of scale-dependent forces (such as the crossing of buoyancy and inertia forces at $l \sim 22$ in figure 5*e*) to dynamically relevant length scales (e.g. Schwaiger *et al.* 2020). However, for high $\widetilde{Ra}_T$ in the WR regime (figure 5*g*), the observed crossings occur at $l \sim 3$, which is much smaller than the dominant wavenumber of the flow ($l \sim 15$, based on the peak of the kinetic energy spectra). Therefore, it may not always be possible to relate crossings of scale-dependent forces to dynamically significant length scales.

Compared to the scale-dependent forces, the scale-dependent curled balances do not produce a clear separation of balances (i.e. primary/secondary/tertiary). In the WN regime (figure 5*d*), an AC balance is evident at large scales, while viscous and inertia forces enter the balance at small scales. The curled force magnitudes in the RR regime (figure 5*f*) are comparable at all scales, leading to an IVAC balance in the scale-integrated representation (figure 5*b*). In the WR regime (figure 5*h*), an IC balance is observed at large scales, while the inertia dominates the balance at small scales.

Figure 5 compares scale-integrated and scale-dependent representations of dynamical balances in our simulations. Integrated forces can not capture cross-over scales where they exist, or the general decrease of the buoyancy force and increase of the inertial force with increasing l (e.g. figure 5*e*). Furthermore, integrated quantities generally do not reflect the force balance at the smallest scales of the solution. Nevertheless, the integrated representation quantitatively captures the overall ordering of forces in a single measure that can be easily compared across a large suite of simulations. In comparison, the curled balances are comparatively less scale-dependent, exhibiting neither a clear ordering of the forces nor any distinct cross-over scales (see also Teed & Dormy 2023). Therefore, a scale-integrated analysis (figure 5*b*) is sufficient to represent the curled forces.

3.5. *Ekman number dependence*

We can now consider the general trend in the balance of forces with increasing $\widetilde{Ra}_T$ and decreasing E. The total magnitude of the fluctuating forces and their curls for $E = 10^{-4}$ and $E = 10^{-6}$ increases with $\widetilde{Ra}_T$ (figure 6), exhibiting a similar dependence to their counterparts at $E = 10^{-5}$ (figures 3 and 4). The Coriolis and pressure forces in the primary QG balance become increasingly separated from the secondary forces as E is reduced

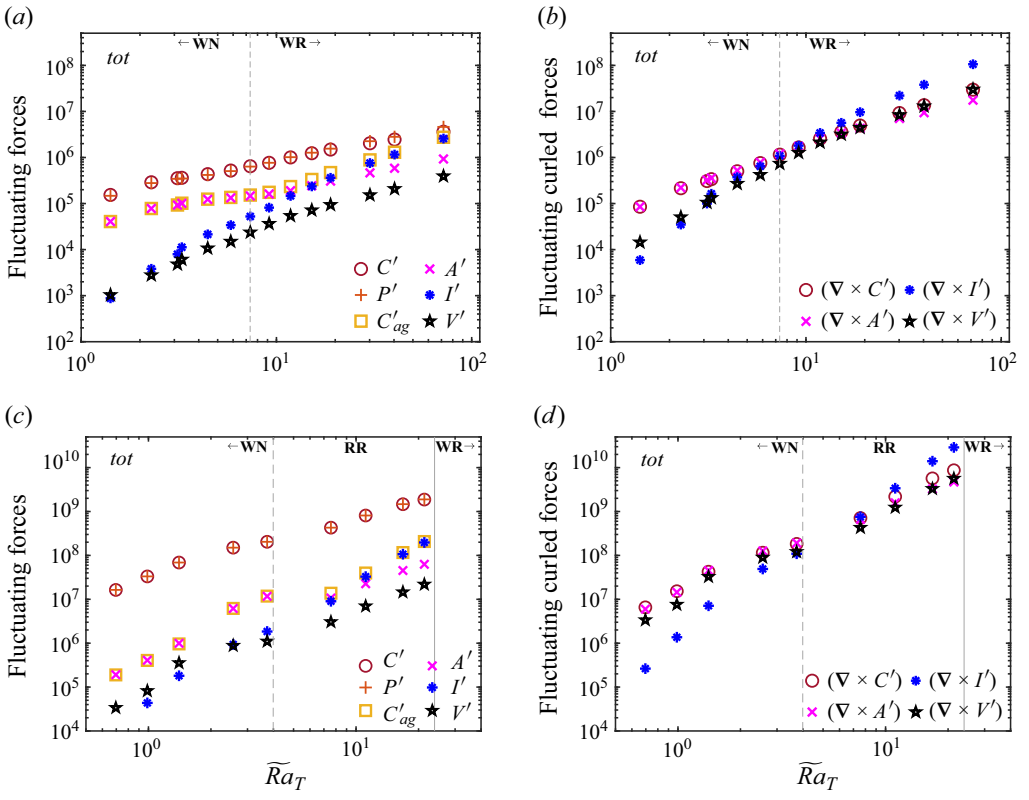

Figure 6. Volume-averaged r.m.s. fluctuating forces (left-hand column) and their curls (right-hand column) at (*a*,*b*) $E = 10^{-4}$ and (*c*,*d*) $E = 10^{-6}$. The dashed vertical line represents the thermal forcing where a transition from WN to WR regimes happens according to the scaling predictions of Long *et al.* (2020). Their analysis does not predict the existence of the RR regime for $E \geqslant 10^{-4}$.

(compare figures 6*a*,*c*). Although the separation between viscous and Coriolis forces increases with decreasing E, the viscous force magnitude remains similar to the other secondary forces. According to asymptotic predictions (Nicoski *et al.* 2024), although the viscous force should decrease compared to Coriolis with decreasing E, the ratio of the viscous force to buoyancy and inertia should remain invariant, which is consistent with our results. The viscous force in the curled balance (figures 6*b*,*d*) also has a magnitude comparable to other curled forces over the investigated range of $\widetilde{Ra}_T$ and E. In summary, we see broadly similar primary and secondary balances in the forces and curled forces at different E, including transitions between dynamic regimes as $\widetilde{Ra}_T$ varies.

4. Summary of dynamical balances and comparison to regimes of L20

Table 1 presents a qualitative summary of the different balances that we found within our suite of simulations depending on whether we considered forces or curled forces, total magnitudes or individual vector components, or partitioning into azimuthally mean and fluctuating contributions. We reiterate here that our analysis reflects bulk dynamics, with the volume averages obtained after removing ten VBLs from each boundary of the domain. Balances similar to those described in detail above for $E = 10^{-5}$ are also found at $E = 10^{-4}$ and $E = 10^{-6}$; the main difference is that the separation between the primary and secondary balances, denoted by a dash (−) in the table, increases with decreasing

	Forces		Curled forces	
Component	Mean	Fluctuating	Mean	Fluctuating
r	$TW - I(TW)_{res}$	$QG - (AC_{ag} \rightarrow IAC_{ag})$	IVC	$VC \rightarrow IVC$
θ	$QG - IC_{ag}$	$QG - (IVC_{ag} \rightarrow IC_{ag})$	IVC	$VAC \rightarrow IVAC$
ϕ	$IVC \rightarrow IC$	$QG - (IVC_{ag} \rightarrow IC_{ag})$	$TW - IV(TW)_{res} \rightarrow IAC$	$VAC \rightarrow IVAC$
tot	$TW - I(TW)_{res}$	$QG - (AC_{ag} \rightarrow IAC_{ag})$	$TW - IV(TW)_{res} \rightarrow IVAC$	$VAC \rightarrow IVAC$

Table 1. Summary of force and curled force balances in our simulations. The ACP balance of forces (or the AC balance of curled forces) is referred to as a TW balance, while the residual of these forces is designated here as $(\mathrm{TW})_{res}$. Similarly, the primary balance between Coriolis and pressure gradient forces is denoted as a QG balance. Primary and secondary force balances are separated by a dash (−), while the changes in the balance with increasing thermal forcing ($\widetilde{Ra}_T$) are designated with a right arrow (→).

Ekman number (e.g. compare figure 5 in this text with figure 3 in supplementary materials S1 and S2). We have tried to denote 'balances' that are groupings of two or more terms that are separated by an order of magnitude in amplitude from other terms; however, such a large separation is not always present. Changes in the balances with $\widetilde{Ra}_T$ are indicated by a right arrow (→), which indicates the general trends with increased thermal forcing but not the specific values at which the balances change. Therefore, table 1 is only a general description of the complex variations in force balances amongst our suite of simulations. In general, increased thermal forcing results in an increase in the relative importance of inertial terms in the balances.

We now compare transitions in the force and curled force balances to previous predictions of regime transitions based on scaling laws (L20). We put emphasis on the $E \leqslant 10^{-5}$ cases as they are more appropriate for comparing with the asymptotic scaling theories used by L20. They defined the WN–RR regime transition (dashed vertical lines in figures 3–5) as $Ra_T = 8Ra_T^c$ based on the observed gradual departure from the linear $Nu - 1 \propto Ra_T/Ra_T^c - 1$ scaling expected just above onset. In the WN regime, they found that the simulated flow length scale ℓ and convective Reynolds number Re_c follow the predictions of VAC theory. L20 defined the RR–WR transition (solid vertical lines in figures 3–5) based on the condition $Ra_T E^{8/5} \sim O(1)$ of Julien *et al.* (2012*a*) above which the thermal boundary layers lose geostrophic balance. They found scalings for ℓ and Re_c close to but statistically different from the predictions of IAC theory.

Figures 3 and 4 show that mean forces exhibit no changes in primary or secondary balances over the range of $\widetilde{Ra}_T$ considered, hence do not conform to the regime transitions found by L20. This is expected, since L20 defined transitions based on quantities that depend strongly on convective fluctuations such as Nu, ℓ and Re_c. In the fluctuating forces, the WN–RR transition correlates with viscous and inertial terms coming into approximate balance with the ageostrophic and buoyancy terms that comprise the secondary balance (figure 5*a*), while in the fluctuating curled forces, this transition arises when the magnitude of the nonlinear advection term becomes comparable to the Coriolis, buoyancy and viscous terms (figure 5*b*). In the fluctuating forces, the RR–WR transition broadly correlates with the amplitude of the viscous term falling below that of the secondary balance, while in the fluctuating curls, this transition appears to correlate with the amplitude of the inertial term rising above the remaining terms. However, the total fluctuating forces and curled forces do not suggest an exact value of $\widetilde{Ra}_T$ where regime transitions occur. Indeed, these quantities exhibit gradual changes with $\widetilde{Ra}_T$ and E (e.g. figures 5(*a*,*b*) and figures 3(*a*,*b*) in both S1 and S2), hence any transition inferred from them is necessarily broad rather than abrupt.

Regime	Forces		Curled forces	
	Mean	Fluctuating	Mean	Fluctuating
WN	$TW - I(TW)_{res}$	$QG - AC_{ag}$	$TW - IV(TW)_{res}$	$VAC \rightarrow IVAC$
RR	$TW - I(TW)_{res}$	$QG - IAC_{ag}$	$TW - IV(TW)_{res} \rightarrow IVAC$	$IVAC$
WR	$TW - I(TW)_{res}$	$QG - IAC_{ag}$	$IVAC$	$IVAC$

Table 2. Summary of force and curled force balances in the regimes of RC simulations as predicted by L20. The balances in total force magnitudes (2.9) have been used here. The abbreviations used here are the same as described in table 1. Primary and secondary force balances are separated by a dash (−), while the changes in the balance with increasing thermal forcing ($\widetilde{Ra}_T$) are designated with a right arrow (→).

Table 2 summarizes the general character of the balances in the regimes defined by L20, calculated using the total magnitude of the mean (supplementary material S3) and fluctuating forces and curled forces. L20 inferred a VAC balance in the WN regime, and an IAC balance in the RR regime, using scaling theory based on the curled force balance. In the WN regime, the calculated fluctuating curled force balance is VAC at low $\widetilde{Ra}_T$, transitioning to an IVAC balance as $\widetilde{Ra}_T$ increases (figure 5*b*). This behaviour is broadly consistent with the assumptions of L20. In the section of the RR regime accessed by our simulations, the calculated fluctuating curled force balance is IVAC rather than the IAC balance assumed by L20. The viscous force is also significant in the force balance (figure 5*a*), though it remains smaller than the other forces in the RR regime. Similar behaviour of the viscous force can also be observed at $E = 10^{-4}$ and $E = 10^{-6}$ (see figures 3(*a*,*b*) in both S1 and S2). Reconciling the calculated dynamical balances in the RR regime with other flow diagnostics such as ℓ, Nu and Re must await a scaling theory for the IVAC regime.

In summary, the fluctuating force and curled force balances exhibit smooth variations over the range of $\widetilde{Ra}_T$ and E considered, reflecting gradual rather than abrupt changes in the dynamics. Broadly speaking, it appears that the RR regime as defined by L20 corresponds to a range of $\widetilde{Ra}_T$ where inertial effects enter the primary fluctuating curled force balance (or the secondary fluctuating force balance). This observation motivated us to seek a single parameter to characterize the changing dynamics with $\widetilde{Ra}_T$. However, it is difficult to find a single quantity that adequately represents the transitions in heat transport and flow behaviour identified by L20. This is perhaps unsurprising given that even the simple VAC scaling laws used by L20 are defined by at least two parameters, while the dominant dynamical balances identified in table 2 involve at least three terms. We therefore classify these balances by introducing two parameters based on our calculated dynamical balances.

Figure 7 shows a quantitative comparison of our dynamical balances with the regime diagram of L20 (their figure 14). To classify the balance in the $E-Ra_T/Ra_T^c$ parameter space, we are motivated by the observation that inertia varies most strongly with $\widetilde{Ra}_T$ in our simulations (figure 5). We therefore introduce two new measures based on the total magnitude of the fluctuating forces and the curled forces (figure 5*a*,*b*) that assess the role of inertia in the force balance.

To measure the degree of geostrophy in the balance we define a force ratio

$$\mathcal{F}_{I/C} = \frac{I'}{C'}. \tag{4.1}$$

We find that the value $\mathcal{F}_{I/C} = 0.1$ can be used to demarcate the simulations belonging to the WR regime as demonstrated in figure 7. Here, $\mathcal{F}_{I/C} > 0.1$ (open symbols) can describe almost all simulations that fall in the WR regime, as compared to the simulations in the range $\mathcal{F}_{I/C} \leqslant 0.1$ (filled symbols) that mostly fall inside the WN and RR regimes.

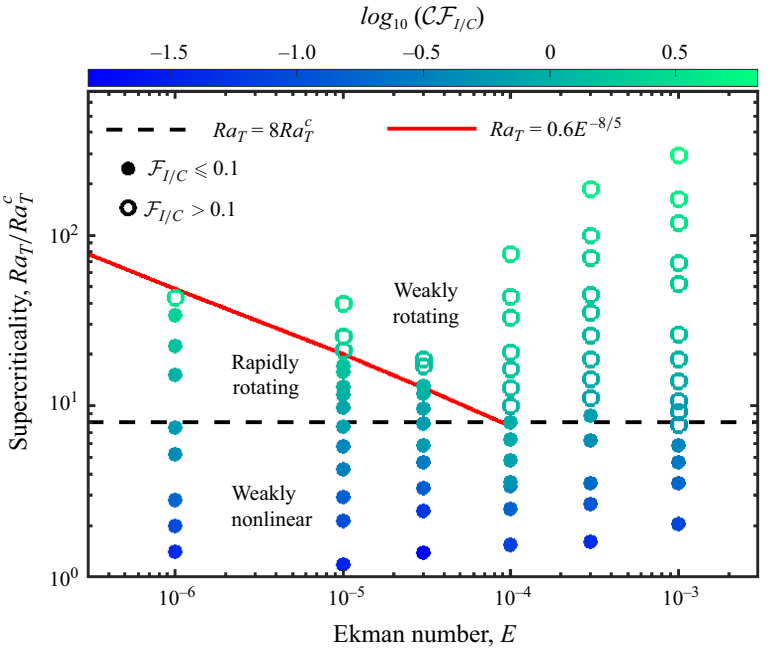

Figure 7. Regime diagram with predicted regime boundaries from the analysis of L20. The primary force balance is classified as QG when $\mathcal{F}_{I/C} \leqslant 0.1$ (filled symbols), and non-QG when $\mathcal{F}_{I/C} > 0.1$ (open symbols). The markers are coloured by $\log_{10}(\mathcal{CF}_{I/C})$. L20 found that the WN–RR regime transition corresponded to the condition $Ra_T/Ra_T^c = 8$, and the RR–WR transition corresponded to the condition $Ra_T = 0.6E^{-8/5}$ of Julien *et al.* (2012*b*).

A comparison can be made between the force ratio $\mathcal{F}_{I/C}$ and the Rossby number $Ro = 2\,Re\,E$ (where Re is the Reynolds number defined in Appendix A), which is often used to represent the ratio of the two forces. We find that the agreement between the magnitudes of $\mathcal{F}_{I/C}$ and Ro worsens as E decreases, and at our lowest E, Ro underestimates $\mathcal{F}_{I/C}$ by approximately a factor of ten.

To measure the role of inertia in the curled balance, we further define a curled force ratio

$$\mathcal{CF}_{I/C} = \frac{\nabla \times I'}{\nabla \times C'}. \tag{4.2}$$

The symbols in figure 7 are coloured by $\log_{10}(\mathcal{CF}_{I/C})$. We emphasize again that the roles of all terms, including inertia, in the dynamical balances change gradually, hence values of $\mathcal{F}_{I/C}$ and $\mathcal{CF}_{I/C}$ that reflect regime transitions must be chosen arbitrarily. Nevertheless, the RR regime can be characterized by the combination of $\mathcal{F}_{I/C} \lesssim 0.1$ and $\log_{10}(\mathcal{CF}_{I/C}) \approx 0$ (i.e. $\mathcal{CF}_{I/C} \approx 1$), which reflects the primary QG balance in the fluctuating forces and the IVAC balance in the fluctuating curled forces, respectively (table 2).

5. Discussion and conclusions

We have analysed different representations of dynamical balances in simulations of spherical shell RC. The radial, co-latitudinal and azimuthal components of the forces have been considered separately to demonstrate the anisotropic nature of dynamical balances. We also partition the forces into azimuthally averaged mean and corresponding fluctuating parts that exhibit distinct balances. Furthermore, the curled force components are also

analysed to investigate the solenoidal force balance. The utility of a scale-dependent representation of curled and uncurled forces has been addressed. Our main findings are presented in figures 3–5 and table 1, and can be summarized as follows.

(i) The bulk curled force balance depends critically on the number of VBLs that are removed near the upper and lower boundaries. We find that removing ten VBLs from each boundary provides a robust estimate of the curled force balance that is broadly consistent with the balance obtained from calculating forces.

(ii) Mean and fluctuating forces and curled forces exhibit distinct balances, consistent with the results of Calkins *et al.* (2021) and Nicoski *et al.* (2024). In particular, the primary mean force and curled force balances are thermal wind (TW), while the primary fluctuating force and curled force balances are quasi-geostrophic (QG) and Inertia–Viscous–Archimedian–Coriolis (IVAC), respectively.

(iii) Radial, co-latitudinal and azimuthal forces exhibit distinct balances as found by Calkins *et al.* (2021) and Aubert (2005) for dynamo simulations. For example, mean forces exhibit a primary TW balance in the radial direction, QG balance in the latitudinal direction, and Inertial–Viscous–Coriolis (IVC) balance in the longitudinal direction. A total force magnitude representation underestimates the role of buoyancy compared to the radial balance.

(iv) In the scale-dependent balances, the separation of magnitude between the forces decreases when a curl operation is performed. Cross-over scales are observed in some but not all force balances, and are not observed in curled force balances, consistent with the results of Teed & Dormy (2023). The curled forces are only weakly scale-dependent and therefore suitably represented by scale-integrated quantities.

(v) Transitions in fluctuating force and curled force balances are broadly consistent with the three regimes of RC obtained by Long *et al.* (2020). However, the relative importance of forces (and their curls) varies gradually with thermal forcing rather than exhibiting any abrupt changes, and therefore does not define precise values of transition parameters.

(vi) The rapidly rotating (RR) regime broadly corresponds to a range of thermal forcing where inertia is of comparable magnitude to the other terms in the primary curled force balance. We find an IVAC rather than an IAC balance in the fluctuating curled forces in the RR regime for the investigated parameter regime (see table 1). Also, the viscous force increases with increasing thermal forcing, and remains significant in the secondary force balance even if E is lowered. These observations are consistent with the predictions of Nicoski *et al.* (2024).

The dynamical balances in table 1 can be compared to results obtained in previous studies. The mean force balance in the dynamo simulations of Calkins *et al.* (2021) with no-slip boundary conditions is TW in the $\hat{r}$ direction and QG in the $\hat{\theta}$ direction, consistent with our results. The mean curled forces in a dynamo simulation with no-slip conditions (Aubert 2005) is also in a TW balance in the azimuthal direction as in our non-magnetic simulations (figure 4*a*). This indicates that the primary mean balance in $\hat{r}$ and $\hat{\theta}$ is consistent between non-magnetic and dynamo simulations, hence is relatively unaffected by the presence of a magnetic field.

The radial fluctuating force behaviour in our no-slip simulations is consistent with the results of Nicoski *et al.* (2024), who observed a primary QG balance in simulations with stress-free boundary conditions. This indicates that the fluctuating balance in non-magnetic RC is not sensitive to the velocity boundary conditions. Notably, the

fluctuating viscous force remains non-negligible within our suite of simulations, similar to the findings of Nicoski *et al.* (2024). Indeed, in the fluctuating curled forces (figure 5*b*), the viscous term is always part of the dominant balance, even at $E = 10^{-6}$ (see figure 3(*b*) in supplementary material S2).

Our scale-dependent force balance in the RR regime is consistent with the balance reported in a previous non-magnetic simulation (Schwaiger *et al.* 2020). Although the scale-dependent force balance does not always exhibit a clear cross-over between forces in all regimes in RC, we find a cross-over between buoyancy and inertia forces in the secondary balance in the RR regime (figures 5(*e*) and 3(*e*) in S1 and S2). However, as observed previously by Teed & Dormy (2023), such cross-overs are not found in the scale-dependent curled balance (figures 5(*f*) and 3(*f*) in S1 and S2). This can be attributed to the separations among the terms, which reduce owing to the curl operation that removes the dynamically irrelevant gradient part. Also, the viscous force, which is important only in the small-scale force balance (figure 5*e*), is significant at all scales in the curled balance (figure 5*f*). This behaviour of the viscous force remains the same for a lower Ekman number ($E = 10^{-6}$; see figure 3(*f*) in S2). Whether the asymptotic separation among various forces, as demonstrated in the numerical simulations of Nicoski *et al.* (2024), can also be demonstrated for curled forces, requires future simulations at lower Ekman numbers ($E < 10^{-6}$).

We choose to look into the force components in a spherical coordinate system ($\hat{r}$, $\hat{\theta}$, $\hat{\phi}$), which matches the spherical shell geometry that we considered and takes advantage of the spherical harmonic representation of our numerical implementation. In rotationally constrained convection (i.e. WN and RR regimes), it can also be useful to study the forces in a cylindrical coordinate system ($\hat{s}$,$\hat{\phi}$,$\hat{z}$), where $\hat{s} = \sin\theta\,\hat{r} + \cos\theta\,\hat{\theta}$ is the cylindrical radius, and $\hat{z} = \cos\theta\,\hat{r} - \sin\theta\,\hat{\theta}$ is the vertical axis of rotation. In particular, strong rotation causes the small-scale leading-order motion to be independent of the $\hat{z}$ direction, known as the Taylor–Proudman constraint (Proudman 1916; Taylor 1923). Asymptotically reduced models enforcing this constraint predict the horizontal (i.e. $\hat{\phi}$) viscous force to be large compared to the vertical component ($\hat{z}$). In the supplementary material, we plot the $\hat{z}$-component of mean and fluctuating forces (S4, figure 1) and the curled forces (S4, figure 2) for the three Ekman numbers $E = 10^{-4}$ (*a*,*b*), $E = 10^{-5}$ (*c*,*d*) and $E = 10^{-6}$ (*e*,*f*). The mean vertical (i.e. $\hat{z}$) viscous force (S4, figure 1*c*) in the WN regime can be seen to be approximately one order of magnitude smaller than the azimuthal ($\hat{\phi}$) viscous force (figure 3*e*), which corresponds well with asymptotic theory (e.g. Sprague *et al.* 2006). However, for higher $\widetilde{Ra}_T$ in the RR and WR regimes, we find that the viscous forces have comparable magnitude in all directions. Also, the fluctuating viscous forces do not exhibit any separation between vertical and horizontal directions. It is difficult to draw any direct comparison with the multiscale asymptotic theory of Sprague *et al.* (2006) since the definitions for mean and fluctuating quantities in the theory are different from our partitioning of forces as defined in (2.6), and the Ekman number range in our study may not be low enough to ensure clear separation at all scales.

Another issue related to the incompressibility condition is the vanishing of azimuthal Coriolis force (C_ϕ) when averaged over geostrophic cylinders (i.e. over ϕ and z). This leads to the zonal flow balance between Reynolds stress ($\overline{I_{ff}}^z$) and viscous forces ($\overline{V}^z$). We recover this balance when integrating over geostrophic cylinders that extend to the solid boundaries. Since the incompressibility condition that enforces the vanishing of Coriolis force requires a closed surface, this balance is not recovered for integration over cylinders constrained to the bulk (i.e. excluding the boundary regions). Therefore, this balance is not

recovered for the azimuthal forces in figure 3(*e*), which have been volume-integrated over the bulk by excluding regions near the boundary.

Our analysis does not take into account the temporal variation of dynamical balances (see e.g. Schaeffer *et al.* 2017), though previous studies suggest that these variations are small (Aubert *et al.* 2017). We also do not consider dynamical balances in the boundary layers since we aim to characterize the bulk dynamics that would ultimately be used to extrapolate to the conditions of planetary interiors and can be compared to available observations. Nevertheless, the calculated bulk dynamical balances form a basis for comparison with different theoretical analyses of RC (e.g. Aubert *et al.* 2001; Calkins *et al.* 2021; Nicoski *et al.* 2024). Similar force calculations can be useful to study various dynamical regimes of convection with $Pr \neq 1$ (Calkins *et al.* 2012; Guzmán *et al.* 2021), double-diffusive convection (Tassin *et al.* 2021) or geodynamo simulations (Calkins *et al.* 2021; Mound & Davies 2023).

Supplementary materials. Supplementary materials are available at https://doi.org/10.1017/jfm.2025.259.

Acknowledgements. This work used the ARCHER UK National Supercomputing Service (http://www.archer.ac.uk) and ARC2, part of the high-performance computing facilities at the University of Leeds, UK. We would like to thank J.A. Nicoski and M.A. Calkins for providing the data to validate our force calculations. We gratefully acknowledge two anonymous reviewers for their suggestions that improved this work.

Funding. S.N., C.J.D. and J.E.M. are supported by Natural Environment Research Council research grant NE/W005247/1. A.T.C. and C.J.D. are supported by NE/V010867/1.

Data availability statement. The data that support the findings of this study are openly available in National Geoscience Data Centre (NGDC), British Geological Survey at https://doi.org/10.5285/6c555767-5a85-4f32-9db6-d947b1aa3387.

Declaration of interests. The authors report no conflict of interest.

Author contributions. C.J.D., J.E.M. and S.N. conceptualized and designed the research. S.N. and A.T.C. developed and conducted numerical simulations and analysis. S.N., C.J.D. and J.E.M. wrote the manuscript.

Appendix A. Table of results

A summary of the characteristics of the three new simulations performed in this study is reported in table 3. The model resolution, input parameters and selected output diagnostic quantities complement table 5 of Appendix B of Mound & Davies (2017), and table 12 in the appendix of L20. Here, N is the numerical resolution, which equals both the number of radial points and the maximum spherical harmonic degree and order, and $N_{\delta i}$ and $N_{\delta o}$ are the number of radial points within the VBLs at the inner and outer boundaries, respectively, where the VBL thicknesses are estimated from the linear intersection method as described in § 2.3. Definitions of the Ekman and modified Rayleigh numbers are given in § 2.1. The Reynolds number is defined as $Re = U^* h/\nu = U = \sqrt{2\,KE/V_s}$, where U is the non-dimensional velocity (the asterisk indicates a dimensional quantity), V_s is the shell volume, and $KE = \iiint_{V_s} \boldsymbol{u}\cdot\boldsymbol{u}\,\mathrm{d}V$ is the kinetic energy integral. Here, Re_{pol} is found by retaining only the poloidal velocity in the kinetic energy integral; Re_{zon} is found by retaining only the terms with spherical harmonic order $m = 0$, from the spherical harmonic expansion of the toroidal velocity in the kinetic energy integral; $\mathcal{P}$ is the time average of the buoyancy production throughout the shell; and ϵ_U is the time average of the viscous dissipation throughout the shell.

$\widetilde{Ra}$	Nu	Re	Re_{pol}	Re_{zon}	$\mathcal{P}$	ϵ_U	N	$N_{\delta i}$	$N_{\delta o}$
350	1.65	165.1	96.4	43.0	1.67×10^9	1.67×10^9	144	9	7
550	1.78	229.9	113.9	62.2	2.80×10^9	2.80×10^9	160	10	7
30 000	17.06	2437.7	1211.0	1186.6	1.76×10^{10}	1.22×10^{10}	384	19	18

Table 3. Summary of the three new runs at $E = 10^{-6}$.

E	m_c	$\widetilde{Ra}^c$	Ra_T^c	$\widetilde{Ra}_T^c$
1×10^{-3}	1	6.61	7.98×10^3	0.798
3×10^{-4}	1	8.43	3.39×10^4	0.681
1×10^{-4}	5	16.4	1.98×10^5	0.919
3×10^{-5}	8	20.1	8.09×10^5	0.754
1×10^{-5}	12	24.7	2.98×10^6	0.642
1×10^{-6}	25	41.0	4.95×10^7	0.495

Table 4. Critical values of Rayleigh numbers and the critical wavenumbers at various Ekman numbers.

Appendix B. Table of critical Rayleigh numbers

The critical values of Rayleigh numbers and wavenumber at the onset of thermal convection at various Ekman numbers are listed in table 4. The critical values of Rayleigh numbers are provided for all three definitions used in this paper as defined in § 2.2.

References

Abbate, J.A. & Aurnou, J.M. 2023 Rotating convective turbulence in moderate to high Prandtl number fluids. *Geophys. Astrophys. Fluid Dyn.* **117** (6), 397–436.

Aubert, J. 2005 Steady zonal flows in spherical shell dynamos. *J. Fluid Mech.* **542**, 53–67.

Aubert, J., Brito, D., Nataf, H.-C., Cardin, P. & Masson, J.-P. 2001 A systematic experimental study of rapidly rotating spherical convection in water and liquid gallium. *Phys. Earth Planet. Inter.* **128** (1), 51–74.

Aubert, J., Gastine, T. & Fournier, A. 2017 Spherical convective dynamos in the rapidly rotating asymptotic regime. *J. Fluid Mech.* **813**, 558–593.

Aurnou, J.M., Horn, S. & Julien, K. 2020 Connections between nonrotating, slowly rotating, and rapidly rotating turbulent convection transport scalings. *Phys. Rev. Res.* **2** (4), 043115.

Calkins, M.A., Aurnou, J.M., Eldredge, J.D. & Julien, K. 2012 The influence of fluid properties on the morphology of core turbulence and the geomagnetic field. *Earth Planet. Sci. Lett.* **359–360**, 55–60.

Calkins, M.A., Orvedahl, R.J. & Featherstone, N.A. 2021 Large-scale balances and asymptotic scaling behaviour in spherical dynamos. *Geophys. J. Intl* **227** (2), 1228–1245.

Christensen, U.R., Aubert, J. & Hulot, G. 2010 Conditions for Earth-like geodynamo models. *Earth. Planet. Sci. Lett.* **296** (3–4), 487–496.

Davies, C.J., Gubbins, D. & Jimack, P.K. 2011 Scalability of pseudospectral methods for geodynamo simulations. *Concurrency Comput. Pract. Exp.* **23** (1), 38–56.

Dormy, E. 2016 Strong-field spherical dynamos. *J. Fluid Mech.* **789**, 500–513.

Gastine, T. & Aurnou, J.M. 2023 Latitudinal regionalization of rotating spherical shell convection. *J. Fluid Mech.* **954**, R1.

Gastine, T., Wicht, J. & Aubert, J. 2016 Scaling regimes in spherical shell rotating convection. *J. Fluid Mech.* **808**, 690–732.

Gastine, T., Wicht, J. & Aurnou, J.M. 2015 Turbulent Rayleigh–Bénard convection in spherical shells. *J. Fluid Mech.* **778**, 721–764.

GILLET, N. & JONES, C.A. 2006 The quasi-geostrophic model for rapidly rotating spherical convection outside the tangent cylinder. *J. Fluid Mech.* **554**, 343–369.
GUERVILLY, C., CARDIN, P. & SCHAEFFER, N.B 2019 Turbulent convective length scale in planetary cores. *Nature* **570** (7761), 368–371.
GUZMÁN, A.J.A., MADONIA, M., CHENG, J.S., OSTILLA-MÓNICO, R., CLERCX, H.J.H. & KUNNEN, R.P.J. 2020 Competition between Ekman plumes and vortex condensates in rapidly rotating thermal convection. *Phys. Rev. Lett.* **125** (21), 214501.
GUZMÁN, A.J.A., MADONIA, M., CHENG, J.S., OSTILLA-MÓNICO, R., CLERCX, H.J.H. & KUNNEN, R.P.J. 2021 Force balance in rapidly rotating Rayleigh–Bénard convection. *J. Fluid Mech.* **928**, A16.
HUGHES, D.W. & CATTANEO, F. 2019 Force balance in convectively driven dynamos with no inertia. *J. Fluid Mech.* **879**, 793–807.
JULIEN, K., KNOBLOCH, E., RUBIO, A.M. & VASIL, G.M. 2012*a* Heat transport in low-Rossby-number Rayleigh–Bénard convection. *Phys. Rev. Lett.* **109** (25), 254503.
JULIEN, K., RUBIO, A.M., GROOMS, I. & KNOBLOCH, E. 2012*b* Statistical and physical balances in low Rossby number Rayleigh–Bénard convection. *Geophys. Astrophys. Fluid Dyn.* **106** (4–5), 392–428.
KING, E.M. & BUFFETT, B.A. 2013 Flow speeds and length scales in geodynamo models: the role of viscosity. *Earth Planet. Sci. Lett.* **371–372**, 156–162.
KING, E.M., STELLMACH, S. & BUFFETT, B. 2013 Scaling behaviour in Rayleigh–Bénard convection with and without rotation. *J. Fluid Mech.* **717**, 449–471.
KUNNEN, R.P.J. 2021 The geostrophic regime of rapidly rotating turbulent convection. *J. Turbul.* **22** (4–5), 267–296.
LONG, R.S., MOUND, J.E., DAVIES, C.J. & TOBIAS, S.M. 2020 Scaling behaviour in spherical shell rotating convection with fixed-flux thermal boundary conditions. *J. Fluid Mech.* **889**, A7.
MATSUI, H. *et al.* 2016 Performance benchmarks for a next generation numerical dynamo model. *Geochem. Geophys. Geosyst.* **17** (5), 1586–1607.
MENU, M.D., PETITDEMANGE, L. & GALTIER, S. 2020 Magnetic effects on fields morphologies and reversals in geodynamo simulations. *Phys. Earth Planet. Inter.* **307**, 106542.
MOUND, J.E. & DAVIES, C.J. 2017 Heat transfer in rapidly rotating convection with heterogeneous thermal boundary conditions. *J. Fluid Mech.* **828**, 601–629.
MOUND, J.E. & DAVIES, C.J. 2023 Longitudinal structure of Earth's magnetic field controlled by lower mantle heat flow. *Nat. Geosci.* **16** (4), 380–385.
NASKAR, S. & PAL, A. 2022*a* Direct numerical simulations of optimal thermal convection in rotating plane layer dynamos. *J. Fluid Mech.* **942**, A37.
NASKAR, S. & PAL, A. 2022*b* Effects of kinematic and magnetic boundary conditions on the dynamics of convection-driven plane layer dynamos. *J. Fluid Mech.* **951**, A7.
NICOSKI, J.A., O'CONNOR, A.R. & CALKINS, M.A. 2024 Asymptotic scaling relations for rotating spherical convection with strong zonal flows. *J. Fluid Mech.* **981**, A22.
OLIVER, T.G., JACOBI, A.S., JULIEN, K. & CALKINS, M.A. 2023 Small scale quasigeostrophic convective turbulence at large Rayleigh number. *Phys. Rev. Fluids* **8** (9), 093502.
ORVEDAHL, R.J., FEATHERSTONE, N.A. & CALKINS, M.A. 2021 Large-scale magnetic field saturation and the Elsasser number in rotating spherical dynamo models. *Mon. Not. R. Astron. Soc. Lett.* **507** (1), L67–L71.
PROUDMAN, J. 1916 On the motion of solids in a liquid possessing vorticity. *Proc. R. Soc. Lond. A Math. Phys. Sci.* **92** (642), 408–424.
ROBERTS, P.H. & KING, E.M. 2013 On the genesis of the Earth's magnetism. *Rep. Prog. Phys.* **76** (9), 096801.
SCHAEFFER, N., JAULT, D., NATAF, H.-C. & FOURNIER, A. 2017 Turbulent geodynamo simulations: a leap towards Earth's core. *Geophys. J. Intl* **211** (1), 1–29.
SCHWAIGER, T., GASTINE, T. & AUBERT, J. 2020 Relating force balances and flow length scales in geodynamo simulations. *Geophys. J. Intl* **224** (3), 1890–1904.
SHEYKO, A., FINLAY, C., FAVRE, J., J, & JACKSON, A. 2018 Scale separated low viscosity dynamos and dissipation within the Earth's core. *Sci. Rep.* **8** (1), 12566.
SODERLUND, K.M., KING, E.M. & AURNOU, J.M. 2012 The influence of magnetic fields in planetary dynamo models. *Earth Planet. Sci. Lett.* **333–334**, 9–20.
SPRAGUE, M., JULIAN, K., KNOBLOCH, E. & WERNE, J. 2006 Numerical simulation of an asymptotically reduced system for rotationally constrained convection. *J. Fluid Mech.* **551**, 141–174.
TASSIN, T., GASTINE, T. & FOURNIER, A. 2021 Geomagnetic semblance and dipolar–multipolar transition in top-heavy double-diffusive geodynamo models. *Geophys. J. Intl* **226** (3), 1897–1919.
TAYLOR, G.I. 1923 Experiments on the motion of solid bodies in rotating fluids. *Proc. R. Soc. Lond. A Math. Phys. Sci.* **104** (725), 213–218.

TEED, R.J. & DORMY, E. 2023 Solenoidal force balances in numerical dynamos. *J. Fluid Mech.* **964**, A26.
WILLIS, A.P., SREENIVASAN, B. & GUBBINS, D. 2007 Thermal core–mantle interaction: exploring regimes for 'locked' dynamo action. *Phys. Earth Planet. Inter.* **165** (1–2), 83–92.
YADAV, R.K., GASTINE, T., CHRISTENSEN, U.R., WOLK, S.J. & POPPENHAEGER, K. 2016 Approaching a realistic force balance in geodynamo simulations. *Proc. Natl Acad. Sci. USA* **113** (43), 12065–12070.